Femto-Joule All-Optical Switching Using Epsilon-Near-Zero High-Mobility Conductive Oxide

Erwen Li and Alan X. Wang, *Senior Member, IEEE*

***Abstract*—Recently discovered extraordinary optical nonlinearities in epsilon-near-zero (ENZ) materials open a new realm of ultra-energy-efficient, all-optical switching devices for future optical communication and computation. In this paper, we propose a sub-micron, sub-pico-second, femto-joule level all-optical switch (AOS) using hybrid plasmonic-silicon waveguides driven by high mobility transparent conductive oxides (HMTCOs) such as cadmium oxide. Our analysis indicates that the ENZ-induced nonlinear optical effect is greatly enhanced by the high free carrier mobility in the telecom wavelength region. We propose an electrically tunable AOS device which is precisely biased at the ENZ condition, or the high-loss "OFF" state. Then the AOS device can be switched to the "ON" state with an unprecedented modulation strength of 15.9 dB/μm and a rapid switching time of 230 fs at the cost of an ultralow switching energy of 13.5 fJ. By defining a comprehensive metric using the product of device size, switching energy and switching time, the proposed ENZ-enabled device shows superior performance than any existing on-chip AOS device. We envision that such HMTCO-driven AOS device can be integrated with silicon photonic integrated circuits to realize on-chip optical signal processing and computation with ultra-low energy and ultra-high bandwidth.**

***Index Terms*—All optical switches, epsilon-near-zero, nonlinear optics, optical computing, photonic integrated circuits, plasmonic waveguides, transparent conductive oxides.**

I. Introduction

OPTICAL computing has resurged in recent years due to the tremendous throughput and low latency superior to the electronic counterpart [1]. While most state-of-the-art optical computing systems adopt hybrid photonic-electronic approaches due to the lack of optical logic gates and optical signal processing units, ultra-fast and energy-efficient all-optical switching (AOS) devices may hold the key to enable true photonic computing systems in the incoming decade [2]. Especially, on-chip AOS devices based on integrated photonics offers the potential for compact size, high density integration, ultra-high bandwidth and energy efficiency. Traditional AOS integrated photonic devices rely on the refractive index change of the waveguide induced by various optical nonlinearities, such as inter-sub-band transition (ISBT) in quantum wells [3]–[6], Kerr effect [7]–[9], band-filling dispersion (BFD) [10], [11], and two-photon-absorption (TPA) [12]. However, such devices require hundreds of microns to millimeters length of waveguide and high-energy input optical signals, which are not suitable for on-chip optical computation and signal processing. The energy consumption and device footprint can be dramatically reduced by microcavities, for example, microring resonators [13]–[16] and photonic crystal (PC) cavities [17]–[20]. Nevertheless, it sacrifices the operational bandwidth due to the elongated photon lifetime, which undermines the most significant advantage of AOS devices. A thorough comparison of most representative on-chip AOS devices can be found at Section IV in this manuscript, which shows a general trade-off between the switching time and energy efficiency. To break such intrinsic limit, it is essential to discover new nonlinear optical effects for AOS devices.

Very recently, transparent conductive oxides (TCOs) have emerged as increasingly favorable tunable materials for active photonic devices because of their unique epsilon-near-zero (ENZ) effect in the telecom wavelength range. The permittivity of TCOs can be engineered over a wide range through tailoring the free carrier concentration [6]. At the ENZ condition, TCO materials experience vanishingly small permittivity and possess intriguing properties such as subwavelength light confinement, enhanced light-matter interactions, slow light effect [21], and extreme nonlinear dispersion [22]. TCO electro-optical devices have been reported including electro-absorption (EA) modulators [23]–[27], micro-resonator modulators [28], [29], and tunable meta-surfaces [30]. For AOS applications, unprecedented nonlinear optical effects have been observed in indium-tin oxide (ITO) [31]–[34], aluminum-zinc oxide (AZO) [35]–[37], and cadmium oxide (CdO) [38], [39]. For example, unit order light-induced refractive index change has been demonstrated in bulk ITO [31], which is beyond the common perturbative description of nonlinear optical response [40]. The nonlinear optical effect in TCOs occurs in the sub-picosecond range, which offers the promise to break the intrinsic limit of switching speed and energy efficiency of AOS devices.

In this paper, we propose the first design of integrated AOS device with femto-joule per bit switching energy based on a hybrid plasmonic-ENZ TCO-silicon waveguide. The innovation of this work comes from the following aspects. First, the low optical loss of the high mobility transparent conductive oxide (HMTCO) enables extremely small absolute permittivity at the

Manuscript received May 13, 2020; revised August 13, 2020; accepted August 17, 2020. Date of publication August 19, 2020; date of current version September 8, 2020. This work was supported by the AFOSR MURI project FA9550-17-1-0071 and the NSF GOALI project 1927271. *(Corresponding author: Alan X. Wang.)*

The authors are with the School of Electrical Engineering and Computer Science, Oregon State University, Corvallis, OR 97331 USA (e-mail: lie@oregonstate.edu; wang@engr.orst.edu).

Color versions of one or more of the figures in this article are available online at https://ieeexplore.ieee.org.

Digital Object Identifier 10.1109/JSTQE.2020.3018104

ENZ condition, resulting in unprecedented ENZ-induced light confinement and optical nonlinearity. Second, the AOS device is electrically tunable by precisely biasing the HMTCO gate to reach the ENZ condition, which ensures high energy efficiency. We theoretically investigated an AOS device driven by CdO with a high electron mobility of 300 cm^2/V·s [38]. It is shown that the device can achieve a giant saturable absorption coefficient of 15.9 dB/μm with an ultra-low saturation energy of 13.5 fJ and an ultrafast switching time of ~230 fs. This high AOS efficiency leads to an ultra-compact device size to be less than 1 μm.

This article is organized in the following order. In Section II, we briefly review the origin of the nonlinear optical effect in TCOs and analyze the relationship between the electron mobility and the ENZ-enhanced nonlinearity. In Section III, we first present the design of a hybrid plasmonic-CdO-silicon waveguide and describe the large electrical tuning range of the device absorption. The AOS device proposed herein operates precisely at the ENZ condition and is initially at the high-loss "OFF" state by the electrical biasing from the gate. Then the AOS device is optically pumped to a low-loss "ON" state due to the heating of the free electrons in the CdO layer. Following that, we describe the transient simulation of the AOS process in the sub-picosecond and femtojoule regime based on the two-temperature model (TTM). In Section IV, we discuss the contribution of electron mobility to the device performance and compare our proposed design with other reported AOS devices by defining a comprehensive metric of device size-switching energy-switching time product.

II. Nonlinear Optical Effects in Epsilon-Near-Zero Transparent Conductive Oxides

A. Ultrafast Carrier-Dependent Nonlinear Optical Effect in Transparent Conductive Oxide

The optical properties of transparent conductive oxide in the telecom wavelength range can be described by the Drude model:

$$\varepsilon = \varepsilon_\infty - \frac{{\omega_p}^2}{\omega^2 + i\omega\Gamma} \tag{1}$$

where ε_∞ is the high-frequency permittivity, Γ is the damping frequency, and ω_p is the plasma frequency, which depends on the material band structure and carrier density, is usually given by

$$\omega_p = \sqrt{\frac{Ne^2}{m_e^*\varepsilon_0}} \tag{2}$$

with N as the electron density and $\mathrm{m_e}^*$ as the effective mass of electron. TCO's optical nonlinearity is induced by the non-parabolicity of the conductive band [33], which means that the electron effective mass $\mathrm{m_e^*}$ in (2) is no longer a constant. A more accurate form of plasma frequency can be written as [32]:

$$\begin{aligned}{\omega_p}^2(E_F,T) = \frac{e^2}{3m_{e0}^*\varepsilon_0\pi^2}\int_0^\infty dE(1+2CE)^{-1} \\ \times\left[\frac{2m_{e0}^*}{\hbar^2}\left(E+CE^2\right)\right]^{\frac{3}{2}}\left[-\frac{\partial f_{FD}}{\partial E}(E_F)\right]\end{aligned} \tag{3}$$

where $\mathrm{m_{e0}}^*$ is the effective mass of electron at the conduction band bottom, C is the non-parabolic parameter of the conduction band, and $(-\partial f_\mathrm{FD}/\partial \mathrm{E})$ is a measure of the thermal broadening of the Fermi-Dirac distribution which is determined by the electron temperature. As a result, the average electron effective mass is a function of both the electron density and electron temperature. When a light pulse propagates through the TCO material, the absorbed photon energy heats up the electron temperature. The dynamics of this thermal process can be quantitatively interpreted by the TTM, which we will discuss in Section III-B. The electron density of TCOs is orders of magnitude smaller than that of noble metals, which leads to smaller electron heat capacitance [31]. Therefore, the electron temperature can experience significant change with moderate photon energy, which induces larger optical nonlinearity. Fig 1a plots the calculated plasmas frequency of CdO as a function of electron density and electron temperature. The material parameters used for calculation are as follows: $\varepsilon_\infty = 5.6$ [41], $\mathrm{m_{e0}}^* = 0.16\ \mathrm{m_0}$[42], $\mathrm{C} = 0.5\mathrm{eV}^{-1}$ [33], and $\mu = 300\ \mathrm{cm^2/V{\cdot}s}$ [38]. We can see that increase in electron temperature decreases the plasma frequency, similar to the decrease in the electron density. Fig 1b plots the permittivity spectra of CdO at different plasma frequencies, which correspond to electron density of $1 \times 10^{20}\ \mathrm{cm^{-3}}$, $8.5 \times 10^{20}\ \mathrm{cm^{-3}}$, $9 \times 10^{20}\ \mathrm{cm^{-3}}$, and $9.5 \times 10^{20}\ \mathrm{cm^{-3}}$ at room temperature (outlined by white lines in fig 1a), respectively. As the plasma frequency increases, the permittivity decreases and the ENZ wavelength, where the real part of permittivity crosses zero, shifts to shorter wavelength and reaches 1.55 μm with electron density of $9.5 \times 10^{20}\ \mathrm{cm^{-3}}$ at the room temperature.

B. Low Loss ENZ HMTCOs and ENZ-Enhanced Optical Nonlinearity

The optical nonlinear process in TCOs involves two steps: absorbing the photon energy and transferring it into electron thermal kinetic energy. Since the conduction band non-parabolic parameters are similar for different TCOs [42], [43], how efficiently the photon energy can be absorbed determines the strength of nonlinear effect of the TCOs. In a typical TCO-based ENZ photonic device, there are two major factors contributing to the absorption of TCO: the intrinsic absorption due to the intra-band absorption and the extrinsic absorption enhancement by the ENZ effect. The intrinsic absorption is described by the Drude model. The imaginary part of the permittivity $\varepsilon^{"}$ is proportional to the damping frequency Γ, $\varepsilon'' \propto \Gamma = q/\mu m_e^*$, which is determined by the electron mobility μ. For different TCOs, the electron mobility can vary over one order of magnitude from 20–30 cm^2/V·s of the lossy TCOs like ITO [44] to over 300 cm^2/V·s of HMTCOs such as CdO [38]. It has been reported that the small free carrier loss enabled by the high electron mobility of HMTCOs can significantly improve the performance of TCO based phase shifters [45]. On the other hand, the extrinsic ENZ-induced absorption enhancement comes from the continuity of electric displacement field. When the electric field is perpendicular to the interface between the TCO and adjacent material, the ratio between the electric field, $\mathrm{E_{TCO}/E_{adjacent}}$, is inversely proportional to the ratio between the absolute permittivity, $|\varepsilon_{\mathrm{TCO}/}\varepsilon_{\mathrm{adjacent}}|$. Thus, the electric

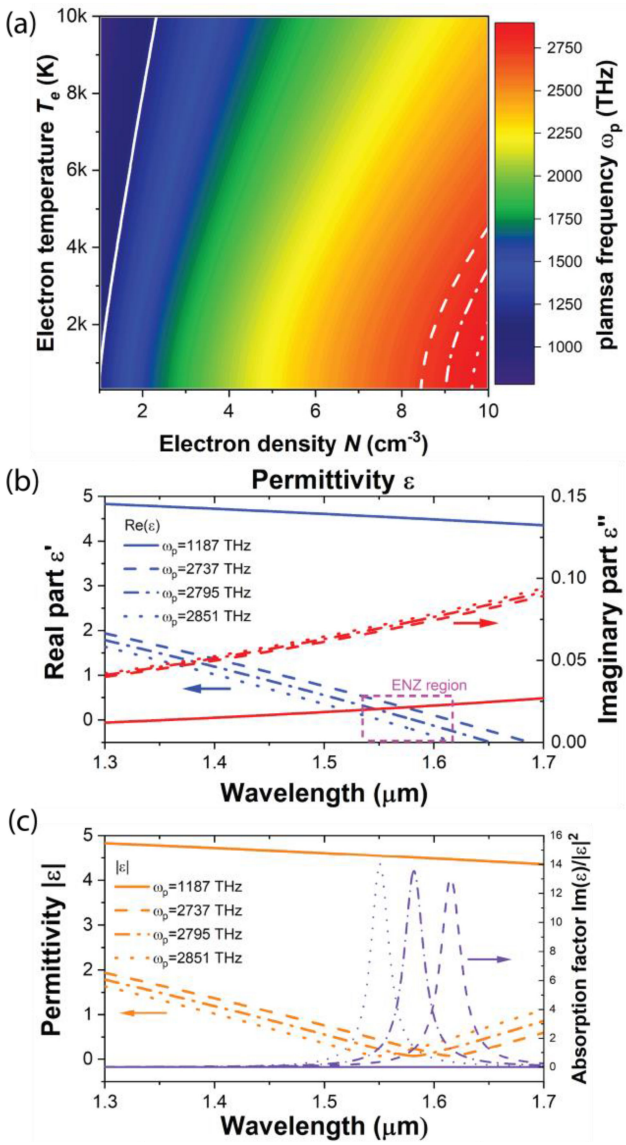

Fig. 1. (a) Plasma frequency of CdO as a function of the electron density and electron temperature. (b) The real and imaginary part of CdO permittivity spectra at different plasma frequencies. (c) Absolute CdO permittivity and absorption factor spectra at different plasma frequencies.

energy will be confined in the TCO at the ENZ condition, enhancing the intrinsic absorption. Based on the dissipation power density in the TCO, $P_d = \omega\varepsilon''\varepsilon_0 E_{TCO}^2/2$, we can define the TCO absorption factor A as $A = \varepsilon''_{TCO}/|\varepsilon_{TCO}|^2 \propto P_d$. When the real part of the permittivity equals zero, the imaginary part dominates the permittivity, $|\varepsilon_{ENZ}| = \varepsilon''_{ENZ}$. Then we have the absorption factor inversely proportional to the imaginary part of the permittivity, $A_{ENZ} = 1/\varepsilon''_{ENZ}$. Interestingly, at the ENZ condition, low loss HMTCO material actually absorbs more photon energy than the lossy TCO material, thus, having larger nonlinear optical effect. Fig 1c plots the absolute permittivity and absorption factor spectra of CdO at different plasma frequencies. We can see that the ENZ-enhanced absorption of CdO is like a low-Q resonant absorber with full width at half maximum of ~20 nm. The peak absorption wavelength red shifts by ~30 nm with a 2% decrease in the plasma frequency, which corresponds to reducing the electron density from 9.5×10^{20} cm^{-3} to 9.0×10^{20} cm^{-3} at the room temperature, or an increase of the electron temperature from room temperature to 2400K for electron density of 9.5×10^{20} cm^{-3}.

III. Ultrafast and Energy-Efficient AOS Based on Plasmonic-CdO-Si Waveguide

A. Device Design and Working Principle

The working principle of the proposed on-chip AOS device depends on the unique design to electrically bias the CdO at the ENZ condition, which brings two exclusive advantages. First, it can guarantee that maximum nonlinear optical effects can be achieved and by tuning the bias voltage, the ENZ wavelength can be dynamically adjusted. Second, the bias voltage will only cause a very thin layer (~1 nm) of accumulation layer while the majority of the CdO layer is still at moderate doping concentration, which will reduce excessive optical waveguide loss. The AOS device initially operates at a high-loss "OFF" state by biasing the CdO at the ENZ condition. Then the device is optically pumped to a low-loss "ON" state due to the increase of free electron temperature by the input optical pulse. Because of the high free electron mobility and the ultra-thin accumulation layer of CdO, the device can be switched with an ultra-high energy efficiency and with an extremely large modulation strength between the "ON" and "OFF" state.

Fig 2a and 2b show the 3D schematic of the AOS device and the 2-D cross-sectional view of the active region of the plasmonic CdO-Si waveguide. The pump and probe light are coupled to the device through a directional coupler for wavelength multiplexing. The active region consists of an Au/CdO/HfO_2/Si capacitor, which is directly coupled to a silicon rib waveguide operating in the transverse electric (TE) mode. The silicon rib waveguide in the center has a height of 250 nm and a width of 300 nm. 40 nm silicon slab provides the conduction path between the waveguide and the metal contact pad. On top of that are 10 nm HfO_2 as the insulator, 10 nm CdO and 100 nm Au as the gate electrode. The fabrication of the device has been described and demonstrated in previous articles, which used similar structures for high speed electro-absorption (EA) modulators [23], [24], [46]. The same processes can be used to fabricate the proposed on-chip AOS device, but with much less stringent requirement on high-speed electrodes. A negative gate bias induces electron accumulation at the CdO/HfO_2 interface. To simplify the analysis, we adopted an uniform electron density approximation for the optical simulation, where the continuous distribution of electron density in the accumulation layer is treated as an equivalent accumulation layer with a uniform electron density distribution over the thickness of the Thomas-Fermi screening length around 1 nm [47]. Compared to non-uniform electron density distribution by quantum moment model [48], the uniform accumulation layer approximation can achieve good accuracy in simulating the peak optical absorption at the ENZ condition of the device with less than 15% error, but greatly simplify the analysis of the AOS device. The relatively big deviation in the required bias voltage between the quantum moment model and uniform accumulation model to reach the ENZ condition is not a concern for AOS devices. Fig 3a plots the loss of the AOS device as a function

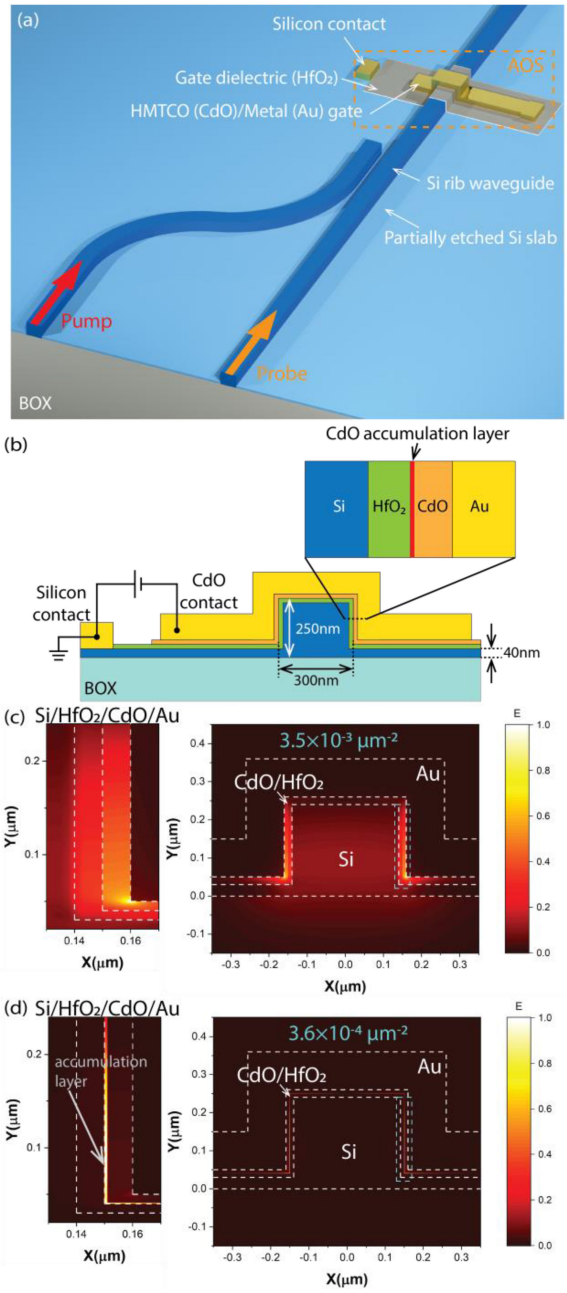

Fig. 2. (a) 3D schematic of the proposed plasmonic-CdO-Si AOS device with the pump and probe light coupling to the device through a directional coupler for wavelength multiplexing. (b) Cross sectional schematic of the active region of the AOS device. (c) and (d) Electric field distribution of the AOS at the (c) zero bias ("ON" state) and (d) ENZ condition ("OFF" state). Inset: zoomed-in electric field distribution at the side wall of the AOS device (cyan dashed box in 2c and 2d).

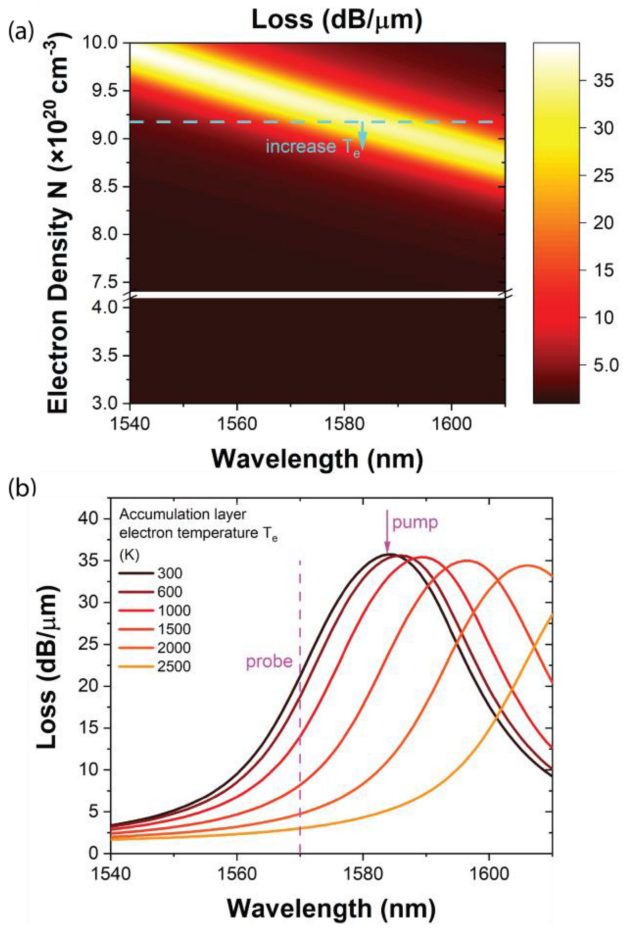

Fig. 3. (a) Optical loss of the AOS device as a function of the wavelength and electron density in the accumulation layer. (b) Optical loss spectra of the AOS with accumulated electron density of 9.18×10^{20} cm^{-3} (dashed line in 3a) at different electron temperatures.

of the accumulated electron density and wavelength. At zero bias, the accumulated electron density equals to the initial bulk electron density of CdO, which is $\sim 3 \times 10^{20}$ cm^{-3}, away from the ENZ region in the telecom wavelength range. The waveguide exhibits an "ON" state with low loss of 1 dB/μm. Finite-difference time-domain (FDTD) simulation shows that the mode conversion loss between the silicon rib waveguide and the "ON" state of plasmonic waveguide is around 0.1 dB/interface. The device loss remains low as the bias increases due to the high electron mobility of CdO until it reaches the "OFF" state at the ENZ condition. When the accumulated electron density increases from 8.78×10^{20} cm^{-3} to 9.75×10^{20} cm^{-3}, the ENZ wavelength is tuned from 1610 nm to 1550 nm. Therefore, we can precisely match the ENZ wavelength with the pump wavelength by controlling the bias to maximize the absorption efficiency and optical nonlinearity. For example, the loss spectrum with electron density of 9.18×10^{20} cm^{-3} (dashed cutline in fig 3a) is plotted in fig 3b, which exhibits an ENZ wavelength of 1585 nm. The peak loss reaches over 35 dB/μm due to the ENZ enhanced absorption. At this condition, if a pump pulse at the ENZ wavelength is coupled into the AOS device, the optical energy will be absorbed efficiently to heat up the electron temperature in the accumulation layer. Fig 3b shows the loss spectra of 9.18×10^{20} cm^{-3} electron density at different electron temperature T_e by assuming the accumulation layer has a uniform electron temperature. As discussed above, increase of the electron temperature has a similar effect as reducing the electron density, which will red-shift the ENZ wavelength. In this case, we can send a probe signal at 1570 nm, achieving both large extinction ratio (ER) and relatively low insertion loss (IL).

Fig 2c and 2d plot the simulated electric field distribution of the AOS device at zero bias ("ON" state) and at the ENZ condition ("OFF" state), respectively. At zero bias, due to the plasmonic effect, the electric field is pulled towards the metal surface from the silicon core and concentrates in the CdO/HfO_2 oxide layer on both side walls of the waveguide. At the ENZ condition, the electric field is dramatically concentrated into the thin CdO accumulation layer due to the ENZ induced field confinement. Strong electric field confinement is especially important for reducing the optical energy consumption of the AOS device. Because the TCO nonlinear effect is quasi-proportional to the optical power intensity [31], [32], more confined optical modes induce larger optical intensity to enhance the nonlinear optical effect. In our design, the AOS device generates an ultra-small mode area of 3.6×10^{-4} μm^2 at the ENZ condition. It produces a power intensity of $\sim$0.15 GW/cm^2 in the accumulation layer with a moderate optical power of 1 mW in the waveguide, which is one order of magnitude larger than the plasmonic effect only, and more than two orders of magnitudes larger than a regular silicon waveguide. In addition, we want to point out that the electrically accumulated 1 nm thick TCO ENZ layer in our AOS device can achieve higher energy efficiency than the conventional bulk stoichiometric doped ENZ TCO [32], which has the entire TCO layer (10 nm thick) at ENZ condition. Because in terms of ENZ induced field confinement, the level of light confinement is also affected by thickness of the ENZ layer, despite the free carrier mobility as discussed above. The light power intensity in the accumulated ENZ layer is $\sim 10\times$ higher than the case of bulk doped ENZ TCO for the same energy input due to thinner ENZ layer thickness, even though the total absorption for latter case is larger.

B. Transient Response of AOS Based on Two-Temperature Model

To evaluate the energy efficiency of the AOS device, we performed transient simulation of the AOS process by integrating the TTM with Lumerical MODE software, which is based on finite difference eigenmode (FDE) method. According to TTM, the evolution of the electrons and lattice temperature can be described by the following equations [31], [32]:

$$\begin{aligned} C_e\frac{\partial T_e(t)}{\partial t} &= -g_{ep}(T_e(t)-T_l(t)) + \frac{N(t)}{2\tau_{ee}(t)},\\ C_l\frac{\partial T_l(t)}{\partial t} &= g_{ep}(T_e(t)-T_l(t)) + \frac{N(t)}{\tau_{ep}(t)},\\ \frac{\partial N(t)}{\partial t} &= -\frac{N(t)}{2\tau_{ee}(t)} - \frac{N(t)}{\tau_{ep}(t)} + P, \end{aligned} \tag{4}$$

Here, N is the energy density stored in the non-thermalized part of the electron distribution, T_e and T_l are the electron and lattice temperature, C_e and C_l are the heat capacity of the electron and lattice, g_{ep} is the electron-phonon coupling coefficient, τ_{ee} and τ_{ep} are the electron-electron and electron-lattice relaxation time, and P is the absorbed power density. The calculation of each parameter can be found in ref [31], [32]. We first extracted the absorbed power density distribution from the eigenmode simulation and plugged into (4). Then, the updated temperature-dependent CdO refractive index distribution was fed back into the eigenmode solver. Repeating this process, we can simulate the change of guided mode properties when a short laser pulse is passing through the AOS device. Because the absorption is majorly confined in the ENZ accumulation layer, we only considered the change of the refractive index in the accumulation layer. We also ignored the thermal diffusion of electrons because in the sub-picosecond time scale, the electron gas heating dominates the time response over the phonon thermal diffusion [49], [50], which has also been verified by the previous TCO-based AOS effect demonstrations [31], [32]. If thermal diffusion were considered, the hot electrons would tend to diffuse away from the accumulation layer, which could shift the ENZ wavelength in the same direction as heating up the electron temperature. The actual switching time would be even shorter. Therefore, it is safe to ignore the thermal diffusion in our analysis.

We chose an accumulation layer with electron density of 9.18×10^{20} cm^{-3} for the transient simulation. A femtosecond pump pulse with a duration of 150 fs at 1585 nm is coupled into the AOS device. Fig 4a shows the evolution of the electron temperature distribution in the CdO accumulation layer at the side wall with the input laser pulse energy of 50 fJ. The cyan curve denotes the incident pump laser pulse. The non-thermal energy stored in the excited electrons acts like a delayed source, heating the electrons and exhibits a quasi-intensity-dependent optical nonlinear effect. Fig 4b plots the loss spectra of the AOS device at the maximum modulation point for different energy of the pump pulse. The AOS provides a broadband nonlinear response near the ENZ wavelength. The pump wavelength reaches the largest ER over 20 dB/μm. The probe wavelength is chosen at 1570 nm since it produces the largest ratio between the ER and IL, which is critical for real applications. We should point out that the irregular shape of the loss spectra at the large input pump energy is because of the different electron temperatures in the accumulation layer as shown in fig 4a. Fig 4c plots the transient response of the AOS device loss at the pump and probe wavelength with different input pulse energy. Generally, the simulation predicts rising time $\sim$100 fs and slightly longer relaxation time, matching the previous reported experimental results [38]. The total switching window is $\sim$230 fs at 100 fJ input energy. It means that the device can potentially operate at a repetition rate over 1Tera bit/s. Fig 4d shows the ER and IL at 1570 nm as a function of input pump energy at different pump wavelength. Clearly, as the input energy increases, the ER increases while the IL decreases. With sufficiently large input pump energy, the AOS device exhibits saturable absorption. To quantitatively analyze the saturable absorption, we fit the AOS device to the following absorption coefficient α:

$$\alpha = \frac{\alpha_S}{1+\left({U}/{U_S}\right)^p} + \alpha_{NS}, \tag{5}$$

where α_S and α_{NS} are the saturable and non-saturable absorption coefficients, which correspond to the maximum ER and minimum IL, respectively, U and U_S are the input pump energy and saturation energy, and p describes the sharpness of the transition.

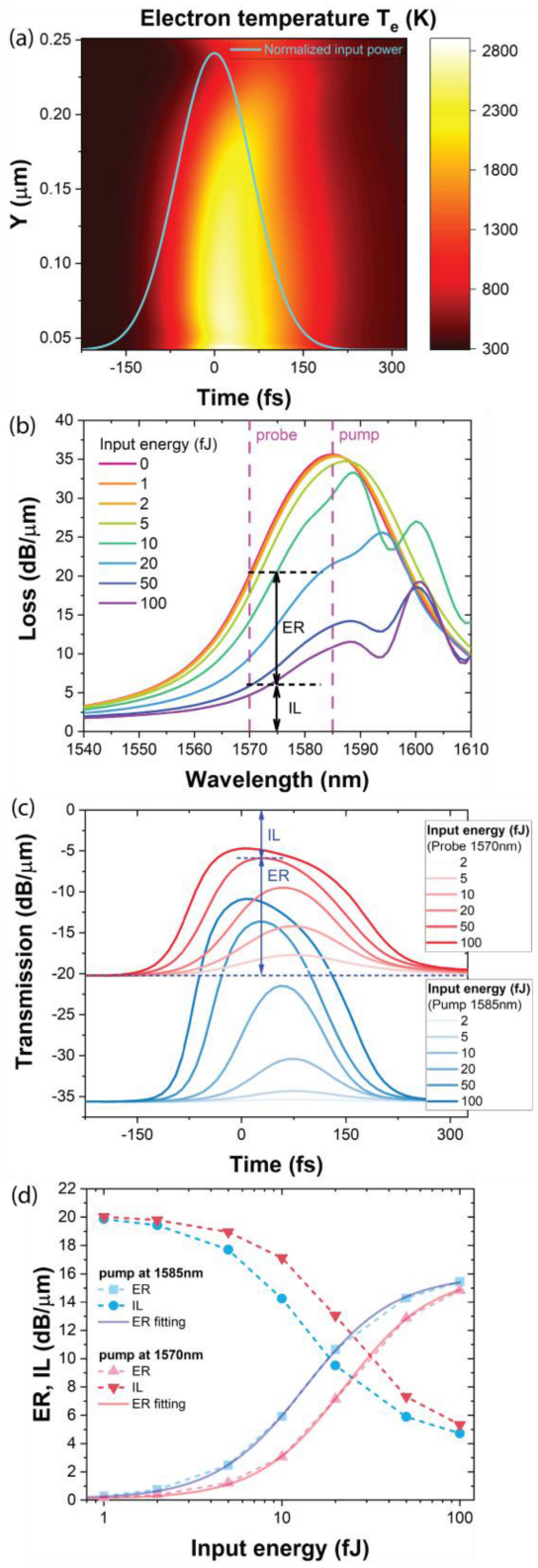

Fig. 4. (a) Simulated evolution of the electron temperature distribution in the CdO accumulation layer at the side wall of AOS device with input pump pulse energy of 50 fJ, assuming the accumulated electron density of 9.18×10^{20} cm^{-3}. The solid curve indicates the input laser pulse profile (arbitrary unit). (b) Loss spectra of the AOS device with different input pump pulse energy. (c) Transient transmission of the AOS device at 1570 nm and 1585 nm with different input pump pulse energy. (d) Extinction ratio and optical loss of the AOS device at 1570 nm as a function of input pulse energy for different pump wavelengths.

TABLE I
CHARACTERISTIC METRICS OF THE DESIGNED AOS

Device length	Footprint	ER	IL	Switching energy	Switching time
330 nm	1.28 μm^2	3 dB	2.4 dB	25 fJ	230 fs

The fitted curve is plotted in fig 4d as solid lines. We derive α_S, α_{NS} and U_S to be 15.9 dB/μm, 4.3 dB/μm, and 13.5 fJ, respectively, which will provide a guidance for the AOS device design. Table I lists the characteristic metrics of an example AOS design. Assuming a length of 330 nm, the AOS device can achieve an ER of ~3 dB and an IL of ~2.4 dB including the mode conversion loss with 25 fJ input energy, but with requirement of pumping the AOS device at the ENZ wavelength. As comparison, if we pump the AOS device away from the ENZ wavelength, for example at the probe wavelength of 1570 nm (red curves in fig 4d), the saturation energy U_S increases from 13.5 fJ to 22.7 fJ due to the reduced absorption efficiency.

Like many AOS devices, power handling capability of our proposed device may be of a concern and should be analyzed. The light intensity at the CdO accumulation layer can be estimated as $I = \frac{1}{2}\varepsilon_0\varepsilon_{TCO}|E|^2 c/n_{eff}$, where c is the light speed, E is the electrical field, and n_{eff} is the effective refractive index of the waveguide mode. Then, assuming an input pump energy of 25 fJ, the peak light intensity at the accumulation layer is calculated to be 35 GW/cm^2 based on the simulated "OFF" state mode profile at ENZ condition. Besides, considering that the accumulation layer has already been heated up and deviates from the ENZ condition before the input pulse reaches maximum, the real peak light intensity may be even smaller. In ref [31], the authors have measured the nonlinear optical response of an ITO thin film with an incident light intensity up to 250 GW/cm^2. Therefore, we anticipate that the CdO at the active region of the AOS device is able to handle the instantaneous light intensity with input pump energy up to the saturation energy.

IV. DISCUSSION

A. The Effect of High Mobility Materials

We have discussed the AOS design based on CdO with a high electron mobility of 300 cm^2/Vs. Similar AOS structure may also apply to other TCO materials. There are other HMTCO materials, such as Ti-doped In_2O_3, which has a mobility ~100 cm^2/Vs [51]. In fact, the electron mobility of CdO itself may also vary from ~30 cm^2/Vs to 600 cm^2/Vs depending on the material process conditions, such as the deposition method, substrate materials, and dopant types [52]–[55]. Here, we compare how the electron mobility of TCOs will affect the performance of the AOS device. Fig 5a plots the optical loss of the AOS device as a function of the accumulation layer electron density for different electron mobilities of 30 cm^2/Vs, 100 cm^2/Vs, and 300 cm^2/Vs by assuming other parameters remaining the same as CdO. We can see that HMTCOs bring two major advantages. First, the peak absorption is proportional to the electron mobility. TCOs with higher mobility can be heated up to higher temperatures

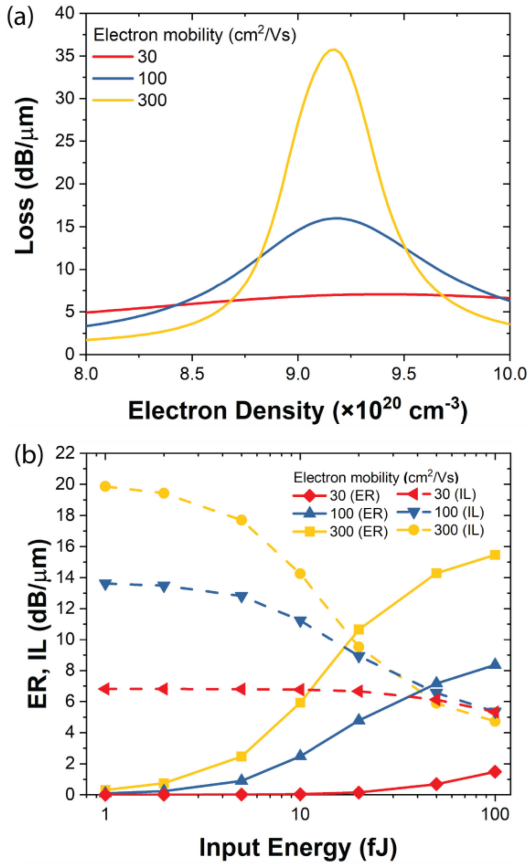

Fig. 5. (a) Optical loss of the AOS device as a function of the accumulation layer electron density for different electron mobilities. (b) Extinction ratio and optical loss of the AOS device at 1570 nm as a function of input pump pulse energy at 1585 nm for different TCO electron mobilities.

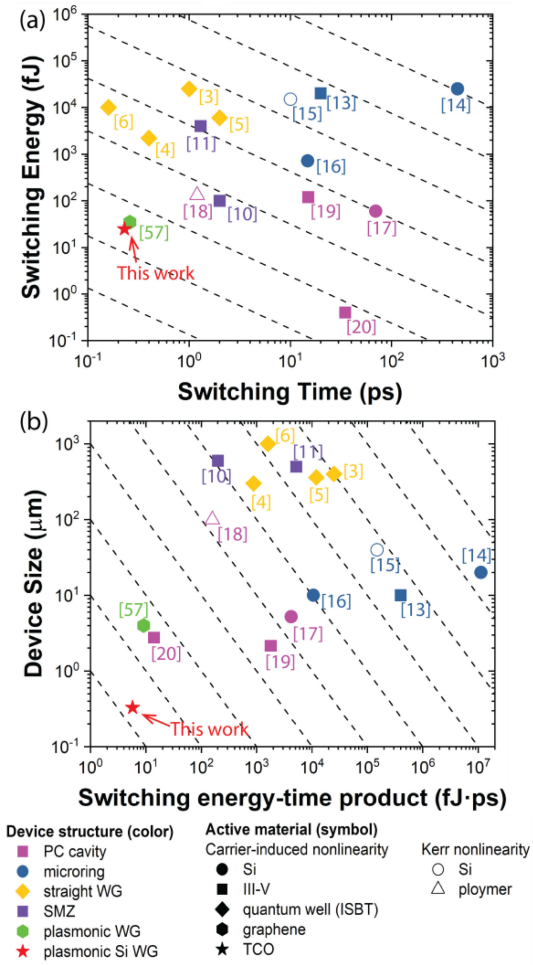

Fig. 6. (a) AOS device performance comparison in terms of switching time and switching energy. (b) AOS device performance comparison in terms switching energy-time product and device size. The color of symbols represents the structure of the AOS devices. The shape of the symbols represents the active material of the AOS devices. The solid symbol indicates carrier-induced nonlinearity, and the hollow symbol indicates Kerr nonlinearity.

due to the larger absorption efficiency at the ENZ wavelength. Second, when the plasma frequency is shifting away from the ENZ condition, the slope of optical loss versus the shift of the plasma frequency is steeper for higher electron mobility. We simulated the AOS nonlinear response with the three electron mobilities. The pump and probe wavelength are kept the same during the simulation. The results are plotted in fig 5b. Generally, reducing the electron mobility from 300 cm^2/Vs to 100 cm^2/Vs, the ER of the AOS reduces by half, and the saturation energy increases around 3 × but still in the femtojoule range. However, for the mobility of 30 cm^2/Vs, the peak absorption is significantly smaller at the ENZ wavelength and it is not sensitive to the change of the accumulation layer electron density. The maximum ER is 3 × smaller than the IL within the simulation range of the input energy. Thus, the energy consumption is significantly higher. Obviously, HMTCO plays a critical role in the operation of the AOS device.

B. Performance Metric: Device Size-Switching Energy-Switching Time Product

The development of future on-chip optical computing systems has raised stringent requirement for AOS devices in terms of device footprint, energy efficiency and switching speed [2]. Here, we define a comprehensive metric of device size-switching energy-switching time product to compare our proposed AOS with other experimentally demonstrated on-chip AOS devices. The results are summarized in fig 6. Fig 6a summarizes the device performances in terms of switching time and switching energy, and fig 6b compares the AOS devices versus switching energy-switching time product and device size. The color and shape of the symbols represent the structure and active material of the AOS devices, respectively. The solid symbol indicates that the AOS is based on a carrier-induced optical nonlinearity, which involves real transitions, such as TPA, single-photon absorption (SPA), BFD, carrier heating and ISBT. While the hollow symbol indicates that the device is based on virtual transition optical nonlinearity, such Kerr effect. Generally, there are two types. The first type is based on light-induced real part change of the refractive index, which requires either a symmetric Mach Zehnder (SMZ) structure [10], [11] or a micro-resonator to convert the phase modulation to intensity modulation. SMZ based AOS can achieve an ultrafast switch on/off time of 2 ps,

by sending two control pulses to the two symmetric branches of the SMZ, despite the relative long carrier recombination time. However, such devices require a long device length of hundreds of microns. For a micro-resonator based AOS device, the Q factor is proportional to the required index shift, which determines the switching energy, and is inversely proportional to the photon lifetime, which limits the switching speed. In this sense, there is a trade-off between energy consumption and the switching speed. For a given material system, the wavelength detune of a resonator is proportional to the ratio between Q factor and mode volume, Q/V_m [56]. Since PC nanocavities offer much better light confinement than microring resonators, the switching energy-switching time product is also significantly smaller. In addition, the carrier-induced nonlinearity in III-V materials is larger than that in Si, therefore, III-V AOS is generally more efficient. To date, the most energy-efficient AOS device was achieved based on InGaAsP 2D PC nanocavity [20] with a switching time of tens of pico-seconds, but impossible to scale to sub-picosecond switching because of the limit of the long carrier lifetime and photon lifetime. The second type of AOS is based on saturable absorption, such as ISBT in semiconductor quantum wells, Pauli blocking of graphene, and the TCO nonlinear effect discussed in this paper. Generally, these nonlinear effects exhibit ultrafast switching time of less than 1ps. The energy efficiency is usually determined by how efficiently the light can be absorbed, which is often related to the light confinement in the active material. Recently, an ultrafast, energy-efficient AOS was demonstrated based on graphene-loaded deep-subwavelength plasmonic waveguide [57]. It reduces the length of device ($\sim 4\mu$m) by 2 orders of magnitude compared with those ISBT AOS, achieving a switching energy of 35 fJ and a switching time of 260 fs. However, the deep-subwavelength plasmonic waveguides induces significant insertion loss and may limit its potential for mass production. For our proposed AOS based on a HMTCO, it exhibits the largest absorption efficiency at the ENZ condition. We can reduce the device length by another order of magnitude to less than 1μm with similar energy consumption as the graphene-loaded plasmonic waveguide. As a result, the proposed AOS device exhibits the smallest device size-switching energy-switching time product, unprecedented for any known design.

V. Conclusion

In summary, we propose a sub-micron, sub-picosecond, femtojoule level AOS device based on an electrically tunable plasmonic-CdO-Si waveguide. Our analysis shows that the high free carrier mobility of CdO plays a critical role in the ENZ-enhanced optical nonlinearity. It ensures the vanishingly small absolute permittivity at the ENZ condition due to the low optical loss, leading to unprecedented optical confinement and enhanced nonlinear optical interaction. Benefited from the electrically tunable design to induce only 1 nm of ENZ layer, the energy efficiency of the device can be maximized by a gigantic saturable absorption coefficient of 15.9 dB/μm with 13.5 fJ energy and a switching time of 230 fs. In addition, this unique design enables a sub-micron compact device size of less than 1 μm, which is essential for advanced optical processing and computing systems such as optical neural network [58]. Our simulation results indicate that HMTCOs play a pivotal role in achieving such superior performance and deserve future experimental investigation. Compared with existing on-chip AOS devices, our proposed HMTCO-driven device shows decisive advantages in terms of the device size-switching energy-switching time product. Furthermore, the AOS device is compatible with silicon photonic integrated circuits. Thus, we anticipate that our proposed HMTCO-driven AOS device will pave a new avenue for future development of ultra-fast, low-power, high-density on-chip optical signal processing and computing systems.

References

[1] Z. Ying *et al.*, "Electronic-photonic arithmetic logic unit for high-speed computing," *Nature Commun.*, vol. 11, no. 1, pp. 1–9, Dec. 2020.

[2] J. Minzioni *et al.*, "Roadmap on all-optical processing," *J. Opt.*, vol. 21, no. 6, 2019, Art. no. 063001.

[3] N. Iizuka, K. Kaneko, and N. Suzuki, "All-optical switch utilizing intersubband transition in GaN quantum wells," *IEEE J. Quantum Electron.*, vol. 42, no. 8, pp. 765–771, Aug. 2006.

[4] G. W. Cong, R. Akimoto, K. Akita, T. Hasama, and H. Ishikawa, "Low-saturation-energy-driven ultrafast all-optical switching operation in (CdS/ZnSe)/BeTe intersubband transition," *Opt. Express*, vol. 15, no. 19, Sep. 2007, Art. no. 12123.

[5] T. Simoyama *et al.*, "Absorption dynamics in all-optical switch based on intersubband transition in InGaAs–AlAs–AlAsSb coupled quantum wells," *IEEE Photon. Technol. Lett.*, vol. 19, no. 8, pp. 604–606, Apr. 2007.

[6] Y. Li, A. Bhattacharyya, C. Thomidis, T. D. Moustakas, and R. Paiella, "Ultrafast all-optical switching with low saturation energy via intersubband transitions in GaN/AlN quantum-well waveguides," *Opt. Express*, vol. 15, no. 26, Dec. 2007, Art. no. 17922.

[7] F. Da Ros *et al.*, "Phase regeneration of DPSK signals in a silicon waveguide with reverse-biased p-i-n junction," *Opt. Express*, vol. 22, no. 5, Mar. 2014, Art. no. 5029.

[8] K. J. A. Ooi *et al.*, "Pushing the limits of CMOS optical parametric amplifiers with USRN:Si 7 N 3 above the two-photon absorption edge," *Nature Commun.*, vol. 8, 2017.

[9] S. Yu *et al.*, "All-optical graphene modulator based on optical Kerr phase shift," *Optica*, vol. 3, no. 5, May 2016, Art. no. 541.

[10] H. Nakamura *et al.*, "Ultra-fast photonic crystal/quantum dot alloptical switch for future photonic networks," *Opt. Express*, vol. 12, no. 26, Dec. 2004, Art. no. 6606.

[11] S. Nakamura, K. Tajima, and Y. Sugimoto, "Experimental investigation on high-speed switching characteristics of a novel symmetric Mach-Zehnder all-optical switch," *Appl. Phys. Lett*, vol. 65, 1994, Art. no. 283.

[12] H. J. S. Dorren *et al.*, "All-optical logic based on ultrafast gain and index dynamics in a semiconductor optical amplifier," *IEEE J. Sel. Top. Quantum Electron.*, vol. 10, no. 5, pp. 1079–1092, Sep. 2004.

[13] T. A. Ibrahim *et al.*, "All-optical switching in a laterally coupled microring resonator by carrier injection," *IEEE Photon. Technol. Lett.*, vol. 15, no. 1, pp. 36–38, Jan. 2003.

[14] V. R. Almeida, C. A. Barrios, R. R. Panepucci, and M. Lipson, "All-optical control of light on a silicon chip," *Nature*, vol. 431, no. 7012, pp. 1081–1084, Oct. 2004.

[15] A. Martínez *et al.*, "Ultrafast all-optical switching in a silicon-nanocrystal-based silicon slot waveguide at telecom wavelengths," *Nano Lett.*, vol. 10, no. 4, pp. 1506–1511, Apr. 2010.

[16] J. S. Pelc *et al.*, "Picosecond all-optical switching in hydrogenated amorphous silicon microring resonators," *Opt. Express*, vol. 22, no. 4, Feb. 2014, Art. no. 3797.

[17] T. Tanabe *et al.*, "Fast all-optical switching using ion-implanted silicon photonic crystal nanocavities," *Appl. Phys. Lett.*, vol. 90, no. 3, Jan. 2007, Art. no. 031115.

[18] X. Hu, P. Jiang, C. Ding, H. Yang, and Q. Gong, "Picosecond and low-power all-optical switching based on an organic photonic-bandgap microcavity," *Nature Photon.*, vol. 2, no. 3, pp. 185–189, Mar. 2008.

[19] C. Husko *et al.*, "Ultrafast all-optical modulation in GaAs photonic crystal cavities," *Appl. Phys. Lett.*, vol. 94, no. 2, Jan. 2009, Art. no. 021111.

[20] K. Nozaki *et al.*, "Sub-femtojoule all-optical switching using a photonic-crystal nanocavity," *Nature Photon.*, vol. 4, no. 7, pp. 477–483, Jul. 2010.
[21] V. E. Babicheva, A. Boltasseva, and A. V. Lavrinenko, "Transparent conducting oxides for electro-optical plasmonic modulators," *Nanophotonics*, vol. 4, no. 1, pp. 165–185, 2015.
[22] O. Reshef, I. De Leon, M. Z. Alam, and R. W. Boyd, "Nonlinear optical effects in epsilon-near-zero media," *Nature Rev. Mater.*, vol. 4, no. 8., pp. 535–551, Jun. 21, 2019.
[23] M. G. Wood *et al.*, "Gigahertz speed operation of epsilon-near-zero silicon photonic modulators," *Optica*, vol. 5, no. 3, p. 233, Mar. 2018.
[24] B. Zhou, E. Li, Y. Bo, and A. Wang, "High-speed plasmonic-silicon modulator driven by epsilon-near-zero conductive oxide," *J. Lightw. Technol.*, pp. 1–1, Mar. 2020.
[25] H. W. Lee *et al.*, "Nanoscale conducting oxide PlasMOStor," *Nano Lett.*, vol. 14, no. 11, pp. 6463–6468, Nov. 2014.
[26] Q. Gao, E. Li, and A. X. Wang, "Ultra-compact and broadband electro-absorption modulator using an epsilon-near-zero conductive oxide," *Photon. Res.*, vol. 6, no. 4, p. 277, Apr. 2018.
[27] A. P. Vasudev, J.-H. Kang, J. Park, X. Liu, and M. L. Brongersma, "Electro-optical modulation of a silicon waveguide with an 'epsilon-near-zero' material," *Opt. Express*, vol. 21, no. 22, Nov. 2013, Art. no. 26387.
[28] E. Li, Q. Gao, S. Liverman, and A. X. Wang, "One-volt silicon photonic crystal nanocavity modulator with indium oxide gate," *Opt. Lett.*, vol. 43, no. 18, Sep. 2018, Art. no. 4429.
[29] E. Li, B. A. Nia, B. Zhou, and A. X. Wang, "Transparent conductive oxide-gated silicon microring with extreme resonance wavelength tunability," *Photon. Res.*, vol. 7, no. 4, p. 473, Apr. 2019.
[30] Y. W. Huang *et al.*, "Gate-tunable conducting oxide metasurfaces," *Nano Lett.*, vol. 16, no. 9, pp. 5319–5325, Sep. 2016.
[31] M. Z. Alam, I. De Leon, and R. W. Boyd, "Large optical nonlinearity of indium tin oxide in its epsilon-near-zero region," *Science (80-.).*, vol. 352, no. 6287, pp. 795–797, May 2016.
[32] M. Z. Alam, S. A. Schulz, J. Upham, I. De Leon, and R. W. Boyd, "Large optical nonlinearity of nanoantennas coupled to an epsilon-near-zero material," *Nature Photon.*, vol. 12, no. 2, pp. 79–83, Feb. 2018.
[33] P. Guo, R. D. Schaller, J. B. Ketterson, and R. P. H. Chang, "Ultrafast switching of tunable infrared plasmons in indium tin oxide nanorod arrays with large absolute amplitude," *Nature Photon.*, vol. 10, no. 4, pp. 267–273, 2016.
[34] P. Guo, R. P. H. Chang, and R. D. Schaller, "Transient negative optical nonlinearity of indium oxide nanorod arrays in the full-visible range," vol. 34, p. 19, 2017.
[35] E. G. Carnemolla *et al.*, "Degenerate optical nonlinear enhancement in epsilon-near-zero transparent conducting oxides," *Opt. Mater. Express*, vol. 8, no. 11, 2018, Art. no. 3392.
[36] L. Caspani *et al.*, "Enhanced nonlinear refractive index in ϵ -near-zero materials," *Phys. Rev. Lett.*, vol. 116, no. 23, 2016.
[37] N. Kinsey *et al.*, "Epsilon-near-zero Al-doped ZnO for ultrafast switching at telecom wavelengths," *Optica*, vol. 2, no. 7, p. 616, 2015.
[38] Y. Yang *et al.*, "Femtosecond optical polarization switching using a cadmium oxide-based perfect absorber," *Nature Photon.*, vol. 11, no. 6, pp. 390–395, Jun. 2017.
[39] S. Saha *et al.*, "Broadband, high-speed, and large-amplitude dynamic optical switching with yttrium-doped cadmium oxide," *Adv. Funct. Mater.*, vol. 30, no. 7, Feb. 2020, Art. no. 1908377.
[40] O. Reshef *et al.*, "Beyond the perturbative description of the nonlinear optical response of low-index materials," *Opt. Lett.*, vol. 42, no. 16, Aug. 2017, Art. no. 3225.
[41] S. Campione *et al.*, "Submicrometer epsilon-near-zero electroabsorption modulators enabled by high-mobility cadmium oxide," *IEEE Photon. J.*, vol. 9, no. 4, pp. 1–7, Aug. 2017.
[42] R. J. Mendelsberg, Y. Zhu, and A. Anders, "Determining the nonparabolicity factor of the CdO conduction band using indium doping and the Drude theory," *J. Phys. D. Appl. Phys.*, vol. 45, no. 42, Oct. 2012.
[43] X. Liu *et al.*, "Quantification and impact of nonparabolicity of the conduction band of indium tin oxide on its plasmonic properties," *Appl. Phys. Lett.*, vol. 105, no. 18, Nov. 2014, Art. no. 181117.
[44] Q. Gao, E. Li, B. Zhou, and A. X. Wang, "Hybrid silicon-conductive oxide-plasmonic electro-absorption modulator with 2-V swing voltage," *J. Nanophoton.*, vol. 13, no. 3, p. 1, Jul. 2019.
[45] I. C. Reines, M. G. Wood, T. S. Luk, D. K. Serkland, and S. Campione, "Compact epsilon-near-zero silicon photonic phase modulators," *Opt. Express*, vol. 26, no. 17, Aug. 2018, Art. no. 21594.
[46] V. J. Sorger, N. D. Lanzillotti-Kimura, R. M. Ma, and X. Zhang, "Ultra-compact silicon nanophotonic modulator with broadband response," *Nanophotonics*, vol. 1, no. 1, pp. 17–22, Jan. 2012.
[47] A. V. Krasavin and A. V. Zayats, "Photonic signal processing on electronic scales: Electro-optical field-effect nanoplasmonic modulator," *Phys. Rev. Lett.*, vol. 109, no. 5, Jul. 2012, Art. no. 053901.
[48] Q. Gao, E. Li, and A. X. Wang, "Comparative analysis of transparent conductive oxide electro-absorption modulators [Invited]," *Opt. Mater. Express*, vol. 8, no. 9, Sep. 2018, Art. no. 2850.
[49] E. Carpene, "Ultrafast laser irradiation of metals: Beyond the two-temperature model," *Phys. Rev. B - Condens. Matter Mater. Phys.*, vol. 74, no. 2, 2006.
[50] J. C. Chow *et al.*, "The dri thermal/optical reflectance carbon analysis system: description, evaluation and applications in U.S. Air quality studies," *Atmos. Environ. Part A, Gen. Top.*, 1993.
[51] M. F. A. M. van Hest, M. S. Dabney, J. D. Perkins, D. S. Ginley, and M. P. Taylor, "Titanium-doped indium oxide: A high-mobility transparent conductor," *Appl. Phys. Lett.*, vol. 87, no. 3, Jul. 2005, Art. no. 032111.
[52] S. K. Vasheghani Farahani *et al.*, "Electron mobility in CdO films," *J. Appl. Phys.*, vol. 109, no. 7, Apr. 2011, Art. no. 073712.
[53] A. A. Dakhel, "Influence of dysprosium doping on the electrical and optical properties of CdO thin films," *Sol. Energy*, vol. 83, no. 6, pp. 934–939, Jun. 2009.
[54] Y. Zhu, R. J. Mendelsberg, J. Zhu, J. Han, and A. Anders, "Transparent and conductive indium doped cadmium oxide thin films prepared by pulsed filtered cathodic arc deposition," *Appl. Surf. Sci.*, vol. 265, pp. 738–744, Jan. 2013.
[55] E. Sachet *et al.*, "Dysprosium-doped cadmium oxide as a gateway material for mid-infrared plasmonics," *Nature Mater.*, vol. 14, no. 4, pp. 414–420, 2015.
[56] E. Li and A. X. Wang, "Theoretical analysis of energy efficiency and bandwidth limit of silicon photonic modulators," *J. Lightw. Technol.*, vol. 37, no. 23, pp. 5801–5813, Dec. 2019.
[57] M. Ono *et al.*, "Ultrafast and energy-efficient all-optical switching with graphene-loaded deep-subwavelength plasmonic waveguides," *Nature Photon.*, 2019.
[58] Y. Shen *et al.*, "Deep learning with coherent nanophotonic circuits," *Nature Photon.*, vol. 11, no. 7, pp. 441–446, Jun. 2017.

Erwen Li received the B.S. degree in physics from Fudan University in 2011, and the Ph.D. degree in electrical and computer engineering from Oregon State University in 2020. His current research interests include transparent conductive oxides integrated novel photonic devices for energy efficient communication and optical computing application.

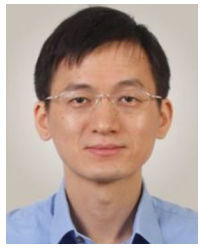

Alan X. Wang (Senior Member, IEEE) received the B.S. degree from Tsinghua University, and M.S. degree from the Institute of Semiconductors, Chinese Academy of Sciences, Beijing, P.R. China, in 2000 and 2003, respectively, and the Ph.D. degree in electrical and computer engineering from the University of Texas at Austin in 2006. From January 2007 to August 2011, he was with Omega Optics, Inc., Austin, Texas, where he served as the Chief Research Scientist with more than 4 million dollars of research grants. Since September 2011, he has been an Assistant Professor at Oregon State University with the School of Electrical Engineering and Computer Science. He was promoted to Associate Professor in September 2017. He has more than 100 journal and 110 conference publications, including 12 invited and plenary presentations. He holds seven issued and pending U.S. patents. He is a Senior Member of IEEE, SPIE, and OSA.